

See discussions, stats, and author profiles for this publication at: <https://www.researchgate.net/publication/244304809>

# Composition and phase changes observed by magnetic resonance imaging during non-solvent induced coagulation of cellulose. Polymer

ARTICLE *in* POLYMER · OCTOBER 2002

Impact Factor: 3.56 · DOI: 10.1016/S0032-3861(02)00531-1

---

CITATIONS

17

---

READS

28

3 AUTHORS, INCLUDING:



[Pete Laity](#)

The University of Sheffield

43 PUBLICATIONS 521 CITATIONS

[SEE PROFILE](#)



[J. N. Hay](#)

University of Birmingham

209 PUBLICATIONS 4,259 CITATIONS

[SEE PROFILE](#)

# Composition and phase changes observed by magnetic resonance imaging during non-solvent induced coagulation of cellulose

P.R. Laity<sup>a,\*</sup>, P.M. Glover<sup>b</sup>, J.N. Hay<sup>c</sup>

<sup>a</sup>*Department of Materials Science and Metallurgy, University of Cambridge, New Museums Site, Pembroke Street, Cambridge CB2 3QZ, UK*

<sup>b</sup>*Magnetic Resonance Centre, School of Physics and Astronomy, University of Nottingham, Nottingham NG7 2RD, UK*

<sup>c</sup>*School of Metallurgy and Materials, University of Birmingham, Edgbaston, Birmingham B15 2TT, UK*

Received 15 May 2002; received in revised form 30 July 2002; accepted 31 July 2002

---

## Abstract

The coagulation of cellulose from solution in *N*-methylmorpholine-*N*-oxide by water was studied by stray field magnetic resonance imaging. Changes in composition and diffusion were readily observable at different depths within the cellulose gel. It was found that the composition changed relatively quickly, due to diffusive exchange of water and solvent, such that cellulose precipitation occurred deep within the bi-phasic region of the phase diagram. The expected spinodal decomposition mechanism was supported by electron microscopic observations of the cellulose morphology. Large increases in diffusion coefficient and relaxation times were attributable to the phase separation and the progressive development of pores within the gel. Moreover, it appeared that the composition changes and evolution of morphology occurred over separate time-scales. © 2002 Published by Elsevier Science Ltd.

**Keywords:** Cellulose morphology; Magnetic resonance imaging; Spinodal decomposition

---

## 1. Introduction

It is widely recognised that the mechanism by which a polymer solidifies from solution plays a major role in defining the resulting morphology. This is particularly important in the manufacture of polymer membranes, since morphology strongly influences the transport properties [1, 2]. In particular, whether the cross-section appears dense or porous on the scale of nanometres to micrometres affects permeability, selectivity and, consequently, the potential applications of the membrane. Dense membranes are generally less permeable but provide more stringent selectivity of smaller species, compared with more porous counterparts.

The various processes that occur during polymer coagulation from solution have, therefore, received much attention. Comprehensive reviews have been given by Van de Witte et al. [3] and Wienk et al. [4]. In general, coagulation can be brought about by different methods involving changes in temperature (thermally induced phase separation), evaporation of a volatile solvent (dry-casting)

or diffusive exchange with a non-solvent (immersion-coagulation or wet-casting). However, while these methods appear outwardly different, they depend on common underlying molecular processes, which can be recognised in terms of the locations on the phase diagram where the phase separation takes place and the corresponding morphologies. These processes are demonstrated in Fig. 1, for a hypothetical polymer/solvent/non-solvent system.

Route A represents vitrification. As the polymer concentration increases, the solution becomes progressively more viscous; chain motion and diffusion slow down and the polymer plus any residual solvent effectively reverts to a glass. This results in a dense morphology with little or no porosity. Vitrification is frequently encountered during ‘dry-casting’, where a volatile solvent is removed by evaporation. However, it may also occur in non-solvent induced coagulation if the ‘outward’ diffusion of solvent is significantly faster than the ‘inward’ diffusion of non-solvent.

In example B, phase separation occurs in the metastable region between the binodal and spinodal lines, at higher polymer concentration than the critical point. Nucleation and growth of non-solvent droplets occurs, which results in the formation of liquid-filled pores in a continuous polymer

---

\* Corresponding author. Tel.: +44-1223-334560.  
E-mail address: [petelaity@aol.com](mailto:petelaity@aol.com) (P.R. Laity).

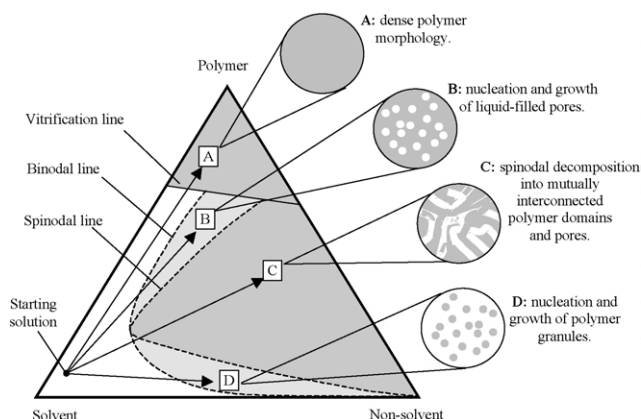


Fig. 1. Isothermal phase diagram of a hypothetical polymer, solvent and non-solvent system showing four coagulation routes and representations of the resulting morphologies.

matrix. This route is common for the immersion-coagulation of many polymer/solvent/non-solvent systems, but can also occur during dry-casting, where a small amount of less volatile non-solvent is included in the polymer solution, along with the more volatile solvent.

In example C, phase separation occurs in the unstable region of the phase diagram, bounded by the spinodal line. Here, polymer-rich and polymer-depleted phases separate initially by the progressive growth of 'concentration waves' of constant wavelength but increasing amplitude, in a process known as 'spinodal decomposition'. This results in a mutually continuous, interwoven network of polymer domains and pores.

Route D enters the metastable region at a polymer concentration below the critical point. In this case, the nucleation and growth of polymer particles produces a granular morphology.

While the above examples have been presented in terms of isothermal composition changes, which may occur during dry- or wet-casting, similar processes can also be described for thermally induced phase separation. Parallels between vitrification as a result of composition change and melt processing are obvious. However, phase separations in other regions of the phase diagram can also be initiated by temperature changes, if a composition is miscible at one temperature but immiscible at another. Examples of this include the upper- or lower critical solution behaviour of some polymer solutions.

In spite of the considerable research effort into non-solvent induced polymer coagulation, a significant problem has been the absence of a suitable method for observing the composition changes taking place within the polymer. Hence, much of the present understanding is based on mathematical models of the diffusive exchange of solvent and non-solvent that are expected during coagulation, along with post-mortem observations of the coagulated polymer morphology. Whilst sophisticated mathematical models have been developed [5–10] doubts can arise as to whether these models adequately reflect the physical processes that

occur during coagulation. Moreover, these models depend on accurate 'in-put' data, concerning diffusion coefficients and how they change with composition, which may not be available for many systems.

We recently demonstrated the capabilities of magnetic resonance imaging (MRI) for following composition and phase changes during polymer coagulation [11]. MRI is a powerful tool for studying both the distribution of liquids in porous or absorbent solids and movement due to flow or diffusion. The basic principles have been described by Callaghan [12], Blümmler et al. [13] and Blümich [14]. By applying a magnetic field gradient across the sample, the resonant frequency of the nuclei under observation (typically protons) encodes for position, while echo attenuation can be used, for example, to determine molecular motion due to diffusion.

The technique of stray field imaging is a variant of MRI, which uses a high permanent magnetic gradient to observe samples in one-dimension [15–17]. This method overcomes many of the problems associated with imaging solid-like systems, which undergo restricted molecular motion, giving relatively fast transverse nuclear relaxations. It can produce relatively high resolution profiles and is particularly useful for observing planar homogeneous structures, which change in one-dimension only. Previous studies include water diffusion in zeolite powder beds [18,19], sandstone rock plugs [20,21] and fibrous cement tiles [22], solvent diffusion in polymers [23,24], the setting of paint films [25] and water diffusion within cellulose membranes [26].

The findings from our MRI investigation of the widely studied cellulose diacetate (CDA)/acetone/water system agreed with previous suggestions [8–10,27] that the coagulation occurred by nucleation and growth of non-solvent filled pores (equivalent to path B in Fig. 1). This work also demonstrated the rapid formation of a relatively impermeable 'skin' of CDA in contact with the coagulant, which restricted the subsequent diffusive exchange of water and acetone. This led to a much slower composition change deeper within the polymer and the formation of larger pores, away from the CDA-bath interface.

In the present work, we have used similar experimental methods to study the different system, based on the coagulation of cellulose from solution in *N*-methylmorpholine-*N*-oxide monohydrate (NMMO/H<sub>2</sub>O). This system is the basis of the lyocell process for making regenerated cellulose fibres and films [28,29] and has been the subject of much previous academic and industrial research. The onset of cellulose solubility appears when the water content of NMMO is less than about 16% by weight [30]; although, for most purposes, a composition close to or slightly dryer than NMMO monohydrate (i.e. 86.7% NMMO and 13.3% water by weight) is used [31–34]. The cellulose can be regenerated from solution by immersion-coagulation in water, which allows the non-solvent to diffuse into the cellulose and NMMO to diffuse out.

The NMMO/cellulose system also well exemplifies the

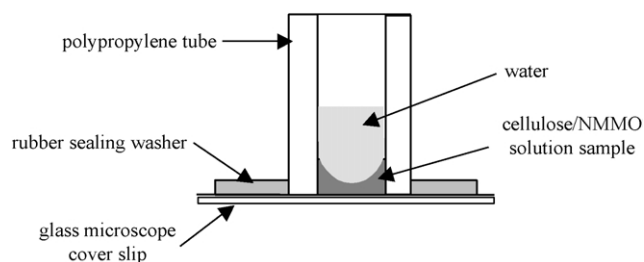


Fig. 2. Sample presentation for MRI experiments.

current position regarding investigations into the evolution of polymer morphology. Much effort has been made to analyse the prevailing sub-microscopic structure of the regenerated cellulose by electron microscopy [35–43] and scattering methods [37–39,41–47]. However, while there has been some study of the effects of solution composition and spinning conditions on the resulting regenerated cellulose [31–34,48–51], there has been little or no investigation into the composition changes which accompany the regeneration process.

## 2. Experimental

### 2.1. Sample preparation

A solution of cellulose was prepared in a mixture of NMMO and water (effectively NMMO monohydrate) by the method of distilling excess water from a slurry, at the UCB Films Research Centre, Wigton, Cumbria. Commercial woodpulp (52 g LV Viscocell, International Paper) was dispersed in a 50% by weight aqueous solution of NMMO (766 g, Huntsman). A small amount of *n*-propyl-3,4,5-trihydroxybenzoate (propyl gallate, 1.3 g, Aldrich) was added as an antioxidant and sequestering agent for iron, to prevent catalytic decomposition of NMMO and the subsequent oxidative depolymerisation of the cellulose [52]. The resulting slurry was transferred to a Z-blade mixer (Winkworth) fitted with a hot oil (set at 105 °C) heating jacket and air-tight lid. Excess water was distilled from the slurry under reduced pressure, over about 90 min, until the cellulose dissolved to give a clear, brown, viscous solution containing approximately 10% cellulose, 79% NMMO, 0.3% PG and 11% water by weight. This solution was poured onto a metal tray and double-wrapped in plastic bags to exclude atmospheric moisture. After allowing it to cool to room temperature, the solution solidified to a glass, which was broken into small lumps, transferred to an air-tight glass jar and stored until required.

Samples for MRI experiments were prepared by re-melting a portion of the NMMO/cellulose solution in an oven at 75 °C and pressing between sheets of polypropylene to a thickness of approximately 150 μm, as determined by a micrometer gauge. After cooling and solidifying again, the resulting film could be cut to size as required. Small portions

were mounted on glass microscope cover slips, as shown in Fig. 2, giving a sample diameter of about 5 mm. These samples were re-melted at 75 °C in an oven, just prior to being used.

### 2.2. MRI measurements

MRI experiments were performed on the GARField system at Surrey University [15], using the methods described previously [11]. Although the imaging methods employed with GARField are similar to pure STRAFI techniques, they are closer to conventional imaging techniques, as the RF pulse excites the whole field of view and the profiles through the sample as a function of depth are obtained by Fourier transform of each echo. Echo-trains consisting of 1 direct echo, followed by 15 further echoes (each a mixture of direct spin-echoes and stimulated echoes), were collected using a pulse sequence defined as

$$\alpha_x - \tau - [\alpha_y - \tau - \text{echo} - \tau]_N - T_R$$

where  $\tau$  was the echo delay time;  $T_R = 250$  ms, the relaxation delay time;  $N = 16$ . The pulse angle is defined as  $\alpha$ , and was arranged to be nominally 90° at the centre of the sample. There was also a spatial dependence of  $\alpha$  due to the planar RF coil, which makes the precise analysis of the echo attenuation difficult. However, the band-width of the RF pulse used exceeded the band-width occupied by the field of view, justifying the simplistic analysis of relaxation and diffusion used. The intensity of the first direct echo was multiplied by 1.5 to compensate for differences in intensity between the direct spin echo and subsequent ‘mixture’ echoes [16]. Each echo was sampled by acquiring 128 points ( $N_p$ ) with a dwell time ( $t_{\text{dwell}}$ ) of 1.6 μs. The resolution of the profile was 6.54 μm, as given by

$$r_{\text{pix}} = \frac{2\pi}{(G\gamma N_p t_{\text{dwell}})} \quad (1)$$

where  $\gamma$  was the magnetogyric ratio for protons ( $2.675 \times 10^8 \text{ s}^{-1} \text{ T}^{-1}$ ) and  $G$  was the magnetic field gradient in the vertical direction ( $17.53 \text{ T m}^{-1}$ ). The profiles based on the first six echoes were averaged to produce a weighted profile. Collecting and averaging 256 scans gave a total scan time of 69 s.

This method gave profiles derived from protons in moderately mobile NMMO and H<sub>2</sub>O within the cellulose gel. Slower moving species, such as the cellulose itself, with transverse relaxation times ( $T_2$ ) much shorter than 120 μs and bulk water with a spin–lattice relaxation time ( $T_1$ ) much longer than 250 ms were selectively excluded from this detection.

A profile of the re-melted NMMO/cellulose solution sample was collected. Then a small amount of water (0.5 ml) was added by dropping pipette and further profiles collected until the signal strength had diminished to the level of background ‘thermal’ noise. The changing quantities of

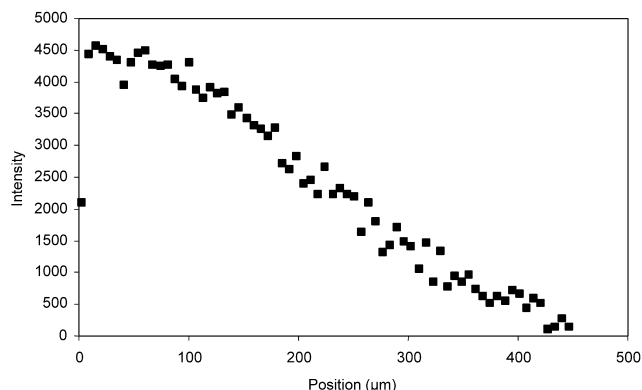


Fig. 3. MRI profile of cellulose/NMMO solution prior to coagulation.

NMMO and water present in the cellulose gel were calculated from the profile intensities during coagulation in  $D_2O$  and  $H_2O$ , assuming a constant proton signal response.

Diffusion coefficients ( $D$ ) and transverse relaxation times were also evaluated by comparing the exponential decay rates of echo trains obtained at two different echo delay times ( $\tau_a = 120$  and  $\tau_b = 300$   $\mu s$ ). For a multi-echo sequence, in a system where the effects of longitudinal relaxation can be ignored (i.e.  $T_1 \ll T_R$ ), the intensities of successive echoes decrease with time ( $t = 2(n - 1)\tau$ , where  $n$  is the echo number) due to the effects of diffusion and transverse relaxation [12–14,16] according to:

$$\ln\left\{\frac{A_t}{A_1}\right\} = -\left(\frac{1}{T_2} + \frac{\gamma^2 G^2 \tau^2 D}{3}\right)t \quad (2)$$

$D$  and  $T_2$  were evaluated from the straight-line plots of  $\ln\{A_t/A_1\}$  against  $t$  using simultaneous equations, giving

$$D = \frac{3(S(\tau_b) - S(\tau_a))}{\gamma^2 G^2 (\tau_a^2 - \tau_b^2)} \quad (3)$$

$$T_2 = \frac{(\tau_a^2 - \tau_b^2)}{(\tau_b^2 S(\tau_a) - \tau_a^2 S(\tau_b))} \quad (4)$$

where  $S(\tau_a)$  and  $S(\tau_b)$  were the slopes corresponding to the two echo delay times. Clearly, these equations are derived assuming perfect  $90^\circ$  RF pulses. However, the simplistic analysis gave good estimates of both  $D$  and  $T_2$  over a wide field of view, when compared to calibration experiments with samples of similar and known parameters, which justifies the approach taken in this work.

In addition, a more accurate, but slower, alternative two-echo sequence with an additional fixed diffusion delay ( $\Delta$ ), written as

$$\alpha_x - \tau - \alpha_y - \tau - \text{echo1} - \tau - (\Delta - 2\tau) - \alpha_y - \tau \\ - \text{echo2} - T_R$$

was also used to measure  $D$  for bulk water, water contained in the freshly coagulated cellulose gel and in NMMO/cellulose solutions prior to the coagulation experiment. Again,

$\alpha$  was set to be nominally  $90^\circ$  within the sample. Measurement of  $D$  for a pure water sample with similar field of view indicated that deviations of the value of  $\alpha$  from  $90^\circ$  that occurred within this experiment were not significant. For each echo, 128 points were acquired and a series of measurements were performed over a range of echo delay times. Values of the diffusion and echo delays were chosen depending on the speed of the diffusion under study. Relatively slow diffusion in the NMMO/cellulose solutions was measured using  $\Delta = 10\,000$  or  $15\,000$   $\mu s$  and  $\tau = 100, 350, 450, 550, 600$  and  $650$   $\mu s$ . In contrast, faster diffusion in the wet cellulose gel was measured using  $\Delta = 700$   $\mu s$  and  $\tau = 100, 150, 175, 200, 225$  and  $250$   $\mu s$ .

For a static field gradient, assuming  $90^\circ$  RF pulses, the decrease in intensity from the first ( $A_1$ ) to second ( $A_2$ ) echoes was given by:

$$A_2 = A_1 \exp\left\{\frac{-\Delta}{T_2}\right\} \exp\{-G^2 \gamma^2 D \Delta \tau^2\} \quad (5)$$

Hence,  $D$  was calculated from the slope ( $S$ ) of the straight-line plot of  $\ln\{A_2/A_1\}$  against  $\tau^2$ , using the equation:

$$D = -\frac{S}{G^2 \gamma^2 \Delta} \quad (6)$$

### 2.3. Electron microscopy

In order to study the regenerated cellulose morphology by scanning electron microscopy (SEM), larger samples of the re-melted cellulose solution were cast onto glass plates and precipitated by immersion in water. The regenerated cellulose samples were dried under constant extension, at room temperature in air, followed by 1 h at  $100^\circ C$  in a vacuum oven. The dried cellulose was notched, using a scalpel, and fractured. Samples were mounted on aluminium sample stubs, using an epoxy adhesive (Araldite), such that the transverse cross-sections were observable. After applying a gold coating, the samples were viewed on a JEOL JSM820 at 20 kV.

Sample preparation for TEM employed a double-fixation method. This method is regarded as standard for plant and animal materials, as discussed by Sabatini et al. [53], and is similar to that used by Iijima et al. [54] for studies of cellulose membranes prepared using the cuprammonium hydroxide solvent system. Water-swollen cellophane was fixed in a buffered (pH 7.2) aqueous solution of glutaraldehyde (2.5%, w/w) and sucrose (1.7%, w/w) for 1 h at  $25^\circ C$ , then post-fixed with osmium tetroxide solution (1%, w/w). Fixed samples were dehydrated by solvent exchange with alcohol, followed by reaction with propylene oxide, then embedded in 'Epon-Araldite' epoxy resin (Agar Scientific Ltd, Stansted). Transverse sections (60 nm thick) were cut using a Reichert-Jung Ultracut ultramicrotome, stained with a mixed aqueous solution of uranyl acetate and lead citrate, then mounted on copper grids. The



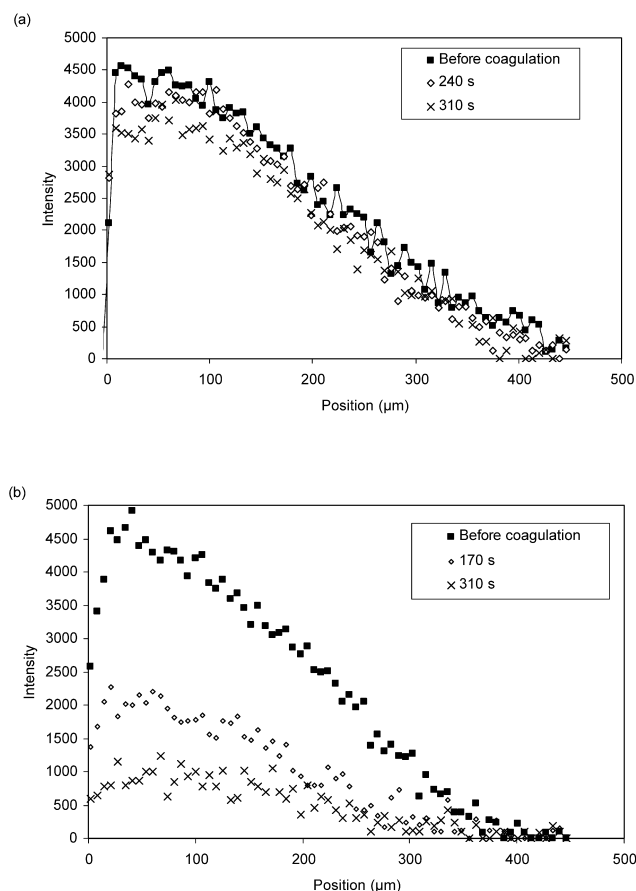


Fig. 4. MRI profiles through cellulose samples during coagulation:  $\tau = 120 \mu\text{s}$ , coagulation times shown in seconds; (a) coagulation in  $\text{H}_2\text{O}$ ; (b) coagulation in  $\text{D}_2\text{O}$ .

samples were viewed on a JEOL JEM-1200EX transmission electron microscope at 60 keV and up to 100 000 $\times$  magnification.

### 3. Results

A MRI profile of a NMMO/cellulose solution sample prior to coagulation is presented in Fig. 3. While the lower edge was relatively sharp, the upper part of the profile appeared to be sloping downwards. There are several possible reasons for this. Some loss of signal strength would be expected as the field of view limit was approached. However, the MRI profile suggested that the re-melted solution sample was thicker than expected. Hence, a more likely explanation was the formation of a meniscus at the upper surface, when the NMMO/cellulose solution sample was re-melted. A similar problem was also experienced during the previously reported study of the CDA/acetone/water system, resulting in some reduction in the capability for spatial resolution of the MRI method.

It was assumed that the observed signal could be related quantitatively, by way of the numbers of protons in each molecule, to the presence of partially constrained  $\text{H}_2\text{O}$  or

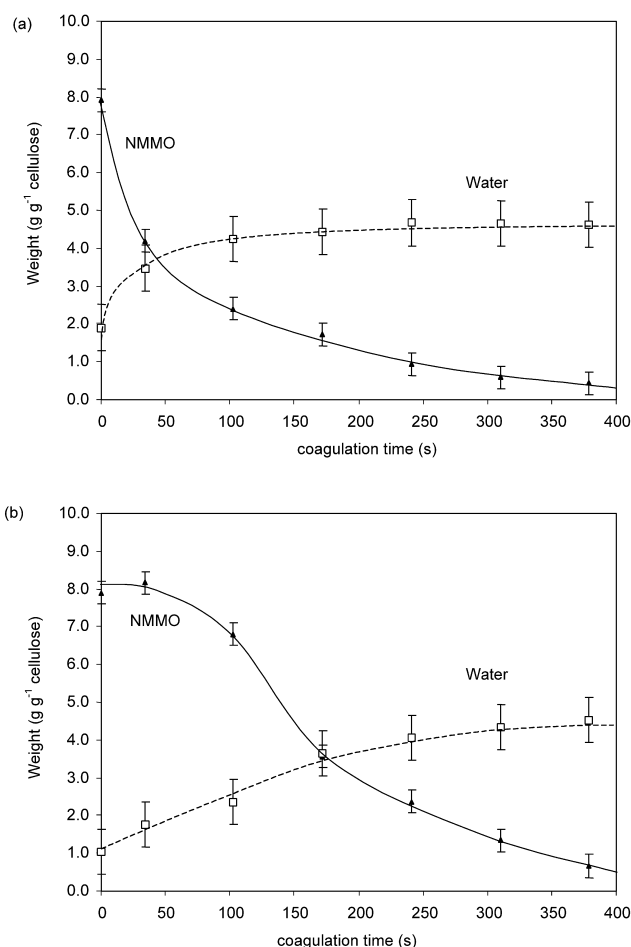


Fig. 5. Calculated changes in NMMO and water content: (a) near the cellulose/water interface; (b) near the middle of the cellulose gel.

NMMO within the cellulose gel. The use of a relatively short relaxation delay time of  $T_R = 0.25 \text{ s}$  suppressed the signal from the bulk aqueous phase, which was expected to have  $T_1$  in the order of several seconds [12]. At the same time, the cellulose was expected to be relatively slow moving, such that its protons had transverse relaxation times less than  $\tau$  and, therefore, too short to contribute to the MRI profiles. Moreover, the anhydroglucose residues, which represented the repeat units of the cellulose chains, accounted for a small mol fraction of the total hydrogen atoms present in the coagulating gel.

#### 3.1. Composition change during coagulation

Fig. 4(a) and (b) shows MRI profiles through samples of precipitating cellulose gel, during the initial 310 s of coagulation in  $\text{H}_2\text{O}$  and  $\text{D}_2\text{O}$ . A relatively small decrease in the profile intensity was observed during the coagulation in  $\text{H}_2\text{O}$ , indicating that diffusion of NMMO out was approximately balanced by diffusion of water into the cellulose. In contrast, coagulation with  $\text{D}_2\text{O}$  was accompanied by a large decrease in the strength of the profile, as NMMO diffused out of the cellulose. Moreover,

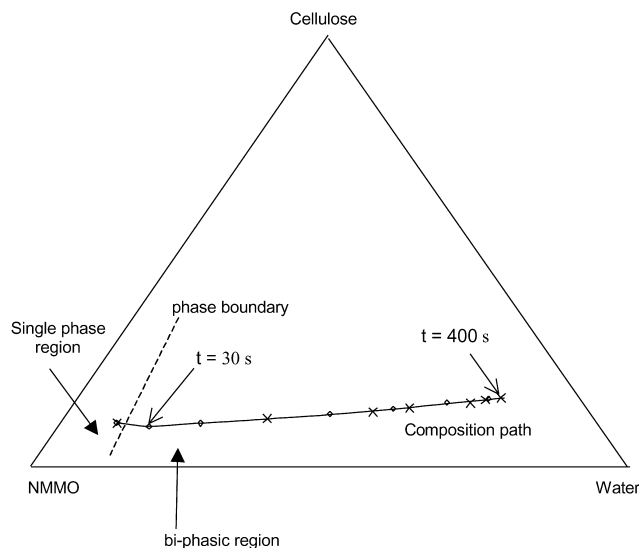


Fig. 6. Composition pathway followed during coagulation; the times indicated correspond to the compositions estimated near the middle of the cellulose gel.

within about 400 s of starting the coagulation in  $D_2O$ , the MRI signal strength had diminished to the level of background noise. It should be noted that these processes were significantly faster than the composition changes noted

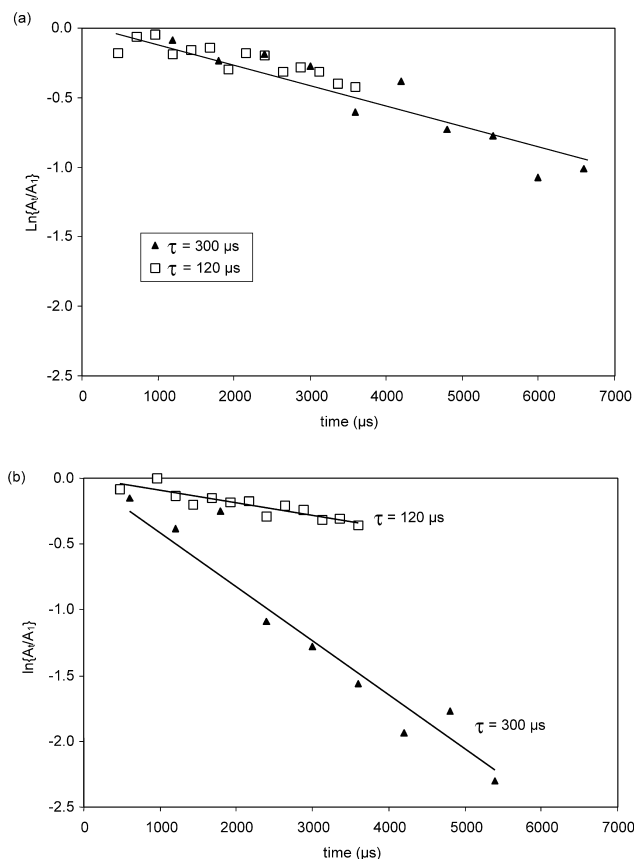


Fig. 7. Echo train decay using 120 and 300  $\mu s$  echo delay times. (a) Prior to starting coagulation; (b) 34 s after start of coagulation.

during coagulation of CDA, which were reported previously.

During  $D_2O$  coagulation, the relative profile intensity was essentially due to protons in NMMO, with relatively minor contributions from the small amounts of  $H_2O$  initially in the sample and the  $D_2O$  used. It was assumed that  $D_2O$  and  $H_2O$  diffused at comparable rates into the coagulating cellulose gel. Hence, the differences between the signal intensities from experiments using  $D_2O$  and  $H_2O$  corresponded to the diffusion of water into the cellulose gel. A conversion factor was derived linking signal strength to the number of protons within each diffusing species, allowing the equivalent weights of NMMO and water contained by 1 g of cellulose to be calculated. It was assumed that cellulose moved relatively little during coagulation. In fact, measurements with a micrometer gauge suggested that the thickness of NMMO/cellulose samples decreased by about 20% during coagulation; however, this effect was not apparent in the MRI studies and has been ignored at present.

The estimated amounts of NMMO and water in the cellulose gel are presented in Fig. 5, for positions near the cellulose/water interface and deeper into the coagulating cellulose gel. The error bars indicated on the NMMO curve ( $\pm 0.16$  g) were obtained directly from the uncertainty in the observed signal strength in Fig. 3; twice this range ( $\pm 0.32$  g) was used to estimate the water content, since this was proportional to the difference between the profile intensities.

Near the cellulose/water interface, the quantities of both water and NMMO began changing immediately on starting the coagulation. In contrast, the changes were more gradual, deeper within the cellulose gel and further away from the coagulant. Moreover, while the water content started to rise immediately, albeit more slowly here than near the interface, the NMMO content appeared to remain unaffected for a period of about 50–100 s, before falling. This suggested that water ingress preceded NMMO egress. However, at both positions within the cellulose gel, the final compositions appeared to be the same. The NMMO content decreased from initially 7.9 g, towards zero beyond 400 s, while the water content rose from a starting level of 1 g to a plateau at about 4.5 g.

These composition changes are also presented in the form of a pathway through the partial phase diagram, in Fig. 6. A complete ternary phase diagram for the cellulose/NMMO/water system is not currently available. However, the location of the phase boundary between the cellulose solution and the bi-phasic region, in the vicinity of the composition path followed, could be estimated from published data [30–34]. This path appeared to cross the phase boundary within the first minute of coagulation and moved deep into the bi-phasic region within 5 min. The slightly faster inward diffusion of water at the start of coagulation initially produced a small decrease in the cellulose concentration. However, the cellulose concentration

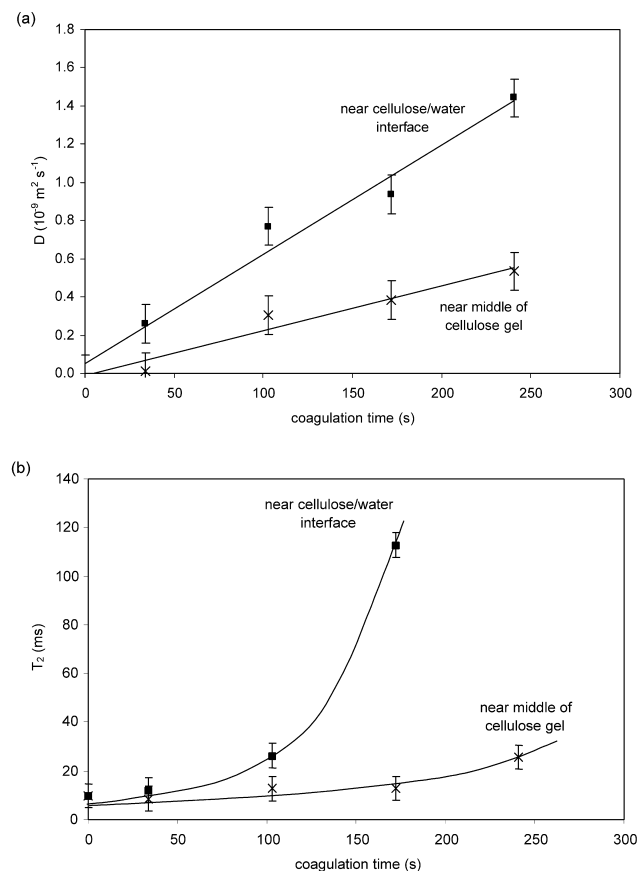


Fig. 8. Changes in (a) diffusion coefficient and (b) relaxation time during coagulation.

then rose during the later stages of coagulation, as the final water level was less than the initial quantity of NMMO.

### 3.2. Diffusion measurements

Prior to adding water to start the coagulation, similar MRI profiles were obtained using pulse sequences with echo delay times of  $\tau = 120$  or  $300 \mu\text{s}$ . Moreover, the plots of  $\ln\{A_t/A_1\}$  against time, using  $\tau = 120$  and  $300 \mu\text{s}$ , indicated

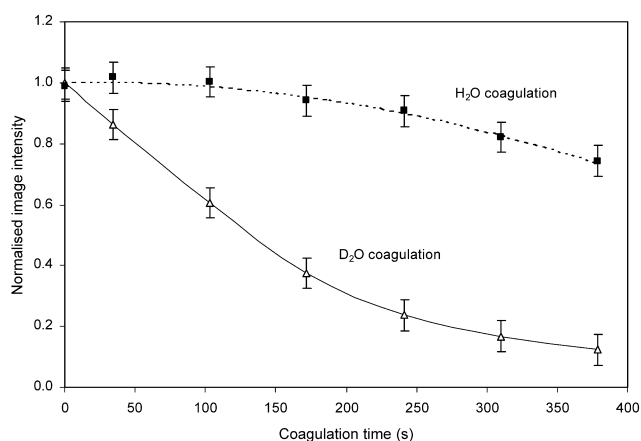


Fig. 9. Change in integrated profile intensity with time.

that the rates of echo decay were roughly similar, with a slope of  $-130 \pm 20 \text{ s}^{-1}$ , as shown in Fig. 7(a). It can be seen from Eq. (2) that the slope depends on  $1/T_2$  and the product  $\tau^2 D$ . Therefore, the similarity in the slopes in Fig. 7(a) suggested negligible diffusion in the initial cellulose solution, with transverse relaxation being the dominant mechanism for the observed decay in echo intensity. From the slope of the linear regression line, a value of  $T_2 = 8.0 \pm 1.3 \text{ ms}$  was estimated.

A more reliable measure of diffusion in the initial NMMO/cellulose solution was given by the two echo method, using Eq. (6) (with  $\Delta = 10$  and  $15 \text{ ms}$ , and  $\tau = 100, 350, 450, 550, 600$  and  $650 \mu\text{s}$ ). This indicated a diffusion coefficient of  $(0.004 \pm 0.001) \times 10^{-9} \text{ m}^2 \text{ s}^{-1}$  in the sample prior to the start of coagulation.

However, after adding  $\text{H}_2\text{O}$ , the stimulated echo train decayed more rapidly with longer echo delay times. This is demonstrated in Fig. 7(b), for a position in the cellulose gel close to the cellulose/water interface. This indicated an increase in diffusion within the coagulated gel.

The changes in diffusion coefficient, calculated from the slopes of  $\ln\{A_t/A_1\}$  against time using Eq. (3), are shown in Fig. 8(a). It was found that  $D$  increased over two orders of magnitude, up to  $(1.5 \pm 0.1) \times 10^{-9} \text{ m}^2 \text{ s}^{-1}$  at the sample surface in contact with the water, within  $240 \text{ s}$  from the start of coagulation. The increase in diffusion coefficient occurred more gradually in the middle of the sample. However, this was interpreted as a delay arising from the distance over which the coagulant had to travel, from the cellulose/water interface to the point of measurement within the sample, rather than a local limit on diffusion. As shown in Fig. 5(a) and (b), the composition changed considerably faster near the interface, compared with deeper within the cellulose gel, and it seems reasonable that this should be mirrored by changes in  $D$ .

The transverse relaxation times were also calculated, using Eq. (4). As shown in Fig. 8(b),  $T_2$  lengthened from about  $8 \pm 1.3 \text{ ms}$  in the NMMO/cellulose solution to a value in excess of  $100 \text{ ms}$ , during the first few minutes of coagulation. This change indicated an increase in the rate of molecular tumbling, during coagulation and was consistent with the increase in diffusion. Again, the change occurred more slowly, deeper within the cellulose gel.

This experiment was curtailed by the loss of MRI signal, which occurred using the longer echo delay times. Only five profiles (equivalent to about  $240 \text{ s}$  coagulation time) could be collected with  $\tau = 300 \mu\text{s}$ , before the signal intensities decreased to background noise levels. This was in sharp contrast to the measurements with  $\tau = 120 \mu\text{s}$ , for which strong signals were obtained for more than  $400 \text{ s}$ . This was attributed to the increase in  $D$ , during coagulation. Since the echo decay rate depended  $\tau^2 D$ , measurements with  $\tau = 300 \mu\text{s}$  were 6.25-times more sensitive to the increase in  $D$  than measurements with  $\tau = 120 \mu\text{s}$ .

Freshly precipitated cellulose was allowed to stand in water overnight, which was expected to allow the gel to



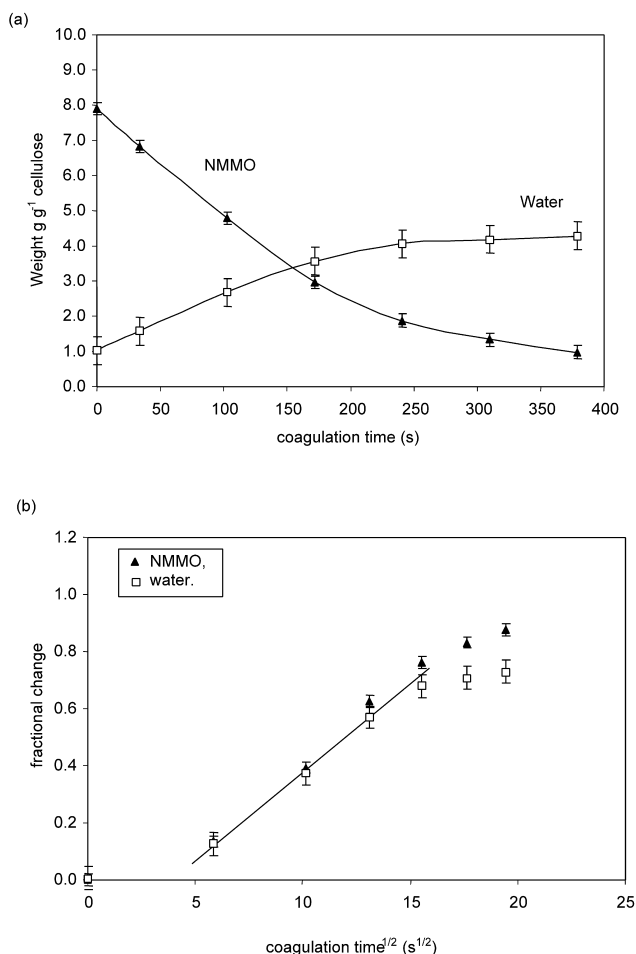


Fig. 10. Change of NMMO and water content in the cellulose gel. (a) Weight fraction vs. time; (b) fractional change vs. time<sup>1/2</sup>.

attain equilibrium and so represent full coagulation. The diffusion coefficient was re-measured using the two echo sequence, with a fixed diffusion delay ( $\Delta = 700 \mu\text{s}$ ) and a series of echo delays ( $\tau = 100, 150, 175, 200, 225$  and  $250 \mu\text{s}$ ). Within the limitations of experimental accuracy,

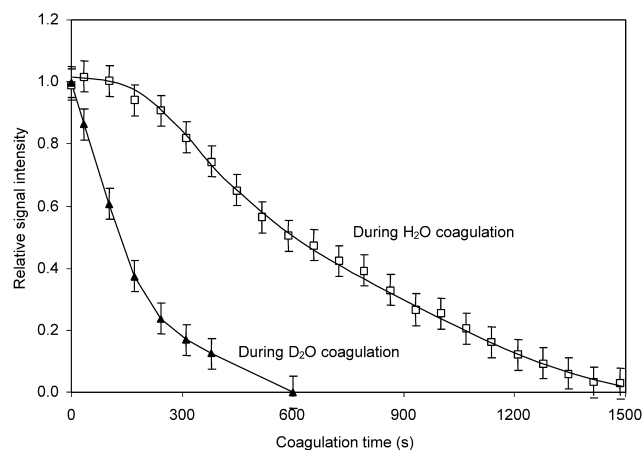


Fig. 11. Change in MRI signal strength over longer coagulation times.

no significant variation in diffusion coefficient was detected across the regenerated cellulose sample. Using averaged data measured near the centre of the gel, the diffusion coefficient was found to be  $(2.0 \pm 0.1) \times 10^{-9} \text{ m}^2 \text{ s}^{-1}$ . This was about 70% of the value measured for bulk water ( $D = 2.85 \times 10^{-9} \text{ m}^2 \text{ s}^{-1}$ ) under the same conditions.

In a separate procedure, the diffusion coefficient was also estimated from the overall composition change, assuming Fickian diffusion and using mathematical models described by Crank [55]. The MRI signal strength was integrated across the entire profile and normalised against the initial value; subsequent changes during coagulations in H<sub>2</sub>O and D<sub>2</sub>O are shown in Fig. 9. The corresponding changes in the total amounts of NMMO and water, calculated from this data, are shown in Fig. 10(a). The error bars were evaluated from the variation of the integrated signal from the first few profiles obtained during the H<sub>2</sub>O experiment, which was about  $\pm 1\%$ .

The fractional changes in NMMO or water contents were defined as

$$F(t) = \frac{W(t) - W_0}{W_\infty - W_0} \quad (7)$$

where  $W(t)$  was the total amount of NMMO or water in the cellulose gel at time  $t$ ,  $W_0$  and  $W_\infty$  were the corresponding values at the start and end of the experiment, respectively.  $F(t)$  is plotted against the square root of time in Fig. 10(b). Non-Fickian behaviour was evident from the change in slope, which occurred at about  $5 \text{ s}^{1/2}$  and represented an increase in the diffusion coefficient after about 25 s during the coagulation. However, a linear, pseudo-Fickian region was observed between  $t^{1/2} = 5$  and  $15 \text{ s}^{1/2}$  (i.e.  $t = 25$ – $225 \text{ s}$ ), from which the effective diffusion coefficients were calculated using the equation [55]

$$D_{\text{eff}} = \frac{\pi h^2 S^2}{4} \quad (8)$$

where  $h$  is sample thickness,  $S$  is the slope and diffusion occurred from one side of the sample only. Within the limits of experimental accuracy,  $D_{\text{eff}}$  for NMMO loss and water influx appeared to be identical. Using a median value for the sample thickness ( $h = 220 \mu\text{m}$ ), Eq. (8) gave  $D_{\text{eff}} = (0.135 \pm 0.010) \times 10^{-9} \text{ m}^2 \text{ s}^{-1}$ .

### 3.3. Loss of signal during H<sub>2</sub>O coagulation

During coagulation experiments in D<sub>2</sub>O, with  $\tau = 120 \mu\text{s}$ , the MRI signal decreased to the level of background noise soon after 5 min, indicative of the exchange of NMMO for water in the cellulose gel. In contrast, the MRI signal from coagulation experiments using H<sub>2</sub>O declined relatively little over this time. However, over a longer period of coagulation, this signal also decreased and eventually disappeared into the background noise, as shown in Fig. 11. This was ascribed to the effect of 'spin saturation' due to the increase in  $T_1$ , which is expected

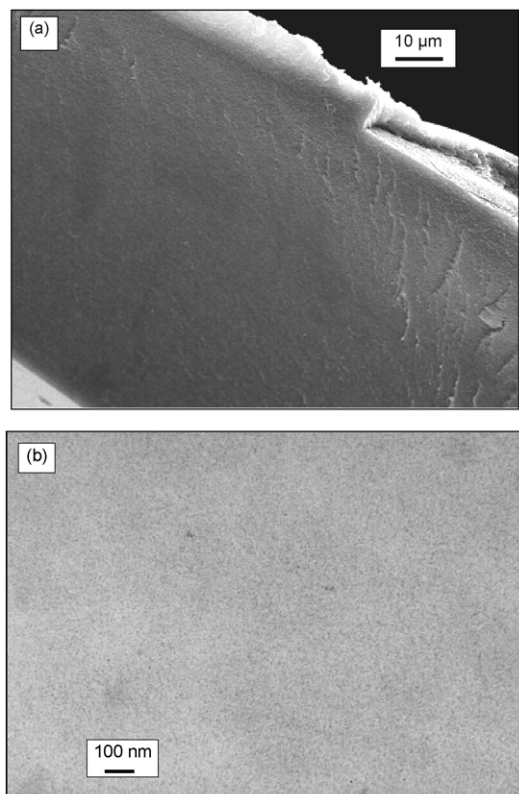


Fig. 12. Observations of regenerated cellulose morphology by (a) SEM, (b) TEM.

to accompany the observed increases in  $D$  and  $T_2$ . For a system where  $T_1$  is comparable to  $T_R$  and much larger than  $\tau$ , the strength of the stimulated echo signal is given by [12–14]

$$A = A_R \left\{ 1 - \exp\left(-\frac{T_R}{T_1}\right) \right\} \quad (9)$$

where  $A_R$  is the signal strength obtained from the system with complete relaxation between scans. The MRI pulse sequence used in this work was deliberately chosen to suppress the signal from bulk water, by using a relatively short relaxation delay of  $T_R = 250$  ms. Although  $T_1$  was not determined directly, it was expected to be equal to or larger than  $T_2$ , which was found to increase beyond 100 ms during the first few minutes of coagulation. Moreover, further increases in relaxation times can be expected, during later stages of the coagulation, in line with the relatively high diffusion coefficient of water observed in the cellulose gel at the end of the coagulation process.

### 3.4. Electron microscopy

Electron micrographs of the regenerated cellulose morphology are presented in Fig. 12. SEM of a cross-section, in Fig. 12(a), showed a few ripples and tears in the fracture surface. However, these were probably caused

when the sample was fractured. Otherwise, the cross-section appeared uniformly dense. No porosity was observable, on the scale of micrometers, in stark contrast to the morphology of precipitated CDA reported previously [11], which was found to be highly porous on this length scale.

A TEM image of a stained, ultramicrotomed section is presented in Fig. 12(b). The heavy metal stain used had no specific affinity for cellulose, but regions of light or heavy staining are believed to indicate variations in permeability of the section. Close examination revealed an interconnected network of lighter and darker regions, which was consistent with porosity on the scale of a few nanometres. Moreover, the structure was reminiscent of that expected to arise from spinodal decomposition, as described by Cahn [56].

## 4. Discussion

This work demonstrates the capabilities of MRI for studying non-solvent induced polymer coagulation. Although the spatial resolution of MRI was adversely affected by sample presentation, composition changes were observable at different positions within the coagulating polymer, which were not amenable to other techniques. In addition, measurements of diffusion coefficient and relaxation times gave information on the morphology of the cellulose gel. This combination of results provided considerable insight into the processes taking place during the coagulation of cellulose from NMMO.

The first stage of coagulation involved diffusive exchange of water and NMMO, in the cellulose. This process occurred relatively quickly, near the cellulose/water interface, and a large composition change was indicated within the first 30 s. However, deeper within the cellulose gel, the exchange took place more slowly and the rise in water content appeared to precede the decrease in NMMO content.

One possible interpretation is that diffusion of the NMMO in the initial cellulose solution was impeded by strong interactions with the polymer. Hydrogen bonding between the N-oxide group and cellulose hydroxyl groups is expected to provide the main solvation mechanism. However, hydrogen bonding is ‘promiscuous’ and can be readily exchanged with other species—in this case, water—releasing the NMMO from the cellulose solvation complex.

As a consequence, the initial precipitation of cellulose appeared to be accompanied by a slight dilution, as the water ingress exceeded the NMMO egress. Later in the coagulation, however, this situation was reversed and the cellulose concentration increased, as a greater volume of NMMO diffused out than water diffused in. The final cellulose concentration in the hydrated gel was higher than in the initial solution used, which corresponded to the shrinkage observed by other means during coagulation.

Relatively slow diffusion and short  $T_2$  times were

observed in the cellulose/NMMO solution prior to coagulation, which were consistent with an intimate association between the polymer and solute. The diffusion coefficient measured in the cellulose/NMMO solution was comparable to values reported by Barton et al. [57] for solutions of poly(ether-sulphone) in dimethylformamide or dimethylsulphoxide. However, an increase in diffusion was observed during the coagulation process, which was too large to be explained merely by diluting the polymer. A more likely explanation was that, as NMMO was displaced from the cellulose solvation complex by the incoming water, phase separation occurred into polymer-rich and polymer-depleted regions. Phase separation was also consistent with the observed increase in  $T_2$  relaxation times. Significantly, these measurements suggested that phase separation started early in the coagulation process, preceding most of the composition change, but continued well after it was complete.

Also, the phase separation appeared to occur well inside the bi-phasic region, where spinodal decomposition was expected to be the dominant mechanism. This was supported by electron microscopy, which indicated that the morphology was composed of interconnected cellulose domains and pores, consistent with spinodal decomposition.

One significant implication of this, with respect to mathematical modelling of coagulation, is that diffusion is controlled by the morphology of precipitated polymer gel, which depends, in turn, on coagulation times, rates and mechanisms of phase separation. Clearly, diffusion is important in controlling composition changes during coagulation. However, as a direct relationship between  $D$  and composition may not exist, this introduces an additional level of complexity, which may not be easily incorporated in mathematical models of coagulation.

That changes in composition and the development of morphology occurred in separate processes became evident during the later stages of coagulation. Although the composition had effectively reached equilibrium, further changes in morphology were implied by the gradual disappearance of the  $H_2O$  signal. This was ascribed to an increase in the  $T_1$  of water within the gel, as 'phase coarsening' of the cellulose-rich and liquid-rich domains progressed. It was not possible to follow these morphological changes in the present work. However, investigations of the development of cellulose morphology during the later stages of coagulation, using simultaneous wide- and small-angle X-ray scattering, will be reported separately.

## 5. Conclusions

MRI is a powerful method for studying non-solvent induced polymer coagulation. Spatially resolved composition measurements were made, which could not be easily obtained by other methods. Furthermore, measurements of

diffusion and relaxation times provided information on the evolving morphology of the coagulating polymer gel.

The coagulation of cellulose from solution in NMMO was found to occur in several stages. Firstly, water diffused into the cellulose/NMMO solution, moving the composition beyond the phase boundary into a bi-phasic region. This initiated phase separation into cellulose-rich and cellulose-depleted domains, with a corresponding increase in diffusion. The third stage involved most of the composition change, as NMMO diffused out and water diffused into the cellulose gel. Finally, after the composition changes were completed, further phase coarsening was implied within the hydrated cellulose gel.

## Acknowledgements

Samples for TEM were prepared by L. Tomkins, of the Biomedical Electron Microscopy Group, University of Birmingham. The work was funded by UCB Films Plc and EPSRC.

## References

- [1] Baker RW. Kirk-Othmer encyclopedia of chemical technology, 4th ed. Membrane Technology, vol. 16.; 1993. p. 135–93.
- [2] Mulder M. Basic principles of membrane technology. Dordrecht, The Netherlands: Kluwer Academic Publishers; 1992.
- [3] Van de Witte P, Dijkstra PJ, van den Berg JWA, Feijen J. *J Membr Sci* 1996;117:1–31.
- [4] Wienk IM, Boom RM, Beerlage MAM, Bulte AMW, Smolders CA, Strathmann H. *J Membr Sci* 1996;113:361–71.
- [5] McHugh AJ, Tsay CS. *J Appl Polym Sci* 1992;46:2011–21.
- [6] Rodovanovic P, Thiel SW, Hwang S-T. *J Membr Sci* 1992;65: 213–29.
- [7] Young T-H, Chen L-W. *J Membr Sci* 1991;59:169–81.
- [8] Tsay CS, McHugh AJ. *J Polym Sci, Part B: Polym Phys* 1990;28: 1327–65.
- [9] Reuvers AJ, Smolders CA. *J Membr Sci* 1987;34:67–86.
- [10] Reuvers AJ, van den Berg JWA, Smolders CA. *J Membr Sci* 1987;34: 45–65.
- [11] Laity PR, Glover PM, Barry A, Hay JN. *Polymer* 2001;42:7701–10.
- [12] Callaghan PT. Principles of magnetic resonance microscopy. Oxford: Clarendon Press; 1991.
- [13] Blümli P, Blümli B, Botto R, Fukushima E. Spatially resolved magnetic resonance. Weinheim: Wiley–VCH; 1998.
- [14] Blümli B. NMR imaging of materials. Oxford: Clarendon Press; 2000.
- [15] Glover PM, McDonald PJ, Newling B. *J Magn Reson* 1997;126: 207–12.
- [16] McDonald PJ. *Prog Nucl Magn Reson Spectrosc* 1997;30:69–99.
- [17] McDonald PJ. *Spectrosc Eur* 1995;7:25–30.
- [18] Hughes PDM, McDonald PJ, Smith EG. *J Magn Reson, Ser A* 1996; 121:147–53.
- [19] Hughes PDM, McDonald PJ, Halse MR, Leone B, Smith EG. *Phys Rev B* 1995;51:11332–8.
- [20] Roberts SP, McDonald PJ, Pritchard T. *J Magn Reson, Ser A* 1995; 116:189–95.
- [21] McDonald PJ. *Magn Reson Imag* 1996;14:807–10.
- [22] Bohris AJ, Newling B, McDonald PJ, Raoof A, Tran NL. *J Mater Sci* 1998;33:859–67.

- [23] Lane DM, McDonald PJ. *Polymer* 1997;38:2329–35.
- [24] Perry KL, McDonald PJ, Randall EW, Zick K. *Polymer* 1994;35:2744.
- [25] Glover PM, Aptaker PS, Bowler JR, McDonald PJ, Ciampi E. *J Magn Reson* 1999;139:90–7.
- [26] Laity PR, Glover PM, Godward J, McDonald PJ, Hay JN. *Cellulose* 2000;7:227–46.
- [27] Stropnik Č, Germeš L, Žerjal B. *J Appl Polym Sci* 1996;61:1821–30.
- [28] Wachsmann U, Diamantoglou M. *Papier* 1997;51:660–5.
- [29] Woodings CR, editor. *Regenerated cellulose fibres*. Cambridge: Woodhead Publishing Ltd; 2000.
- [30] Chanzy H, Noe P, Paillet M, Smith P. *J Appl Polym Sci, Appl Polym Symp* 1983;37:239–59.
- [31] Bang YH, Lee S, Park JB, Cho HH. *J Appl Polym Sci* 1999;73:2681–90.
- [32] Kim SO, Shin WJ, Cho H, Kim BC, Chung IJ. *Polymer* 1999;40:6443–50.
- [33] Andresen EM, Mitchell GR. *Polymer* 1998;39:7127–9.
- [34] Schrempf C, Schild G, Rief H. *Papier* 1995;12:748–57.
- [35] Fink H-P, Purz HJ, Wiegel P. *Papier* 1997;51:643–52.
- [36] Purz HJ, Graf H, Fink H-P. *Papier* 1995;49:714–30.
- [37] Schurz J, Lenz J, Wrentschur E. *Angew Makromol Chem* 1995;229:175–84.
- [38] Schurz J, Lenz J. *Macromol Symp* 1994;83:273–89.
- [39] Lenz J, Schurz J, Wrentschur E. *Colloid Polym Sci* 1993;271:460–8.
- [40] Schurz J, Zipper P, Lenz JJMS. *Pure Appl Chem* 1993;A30:603–19.
- [41] Lenz J, Schurz J, Wrentschur E. *Acta Polym* 1992;43:307–12.
- [42] Lenz J, Schurz J. *Cellul Chem Technol* 1990;24:679–92.
- [43] Lenz J, Schurz J, Wrentschur E. *J Appl Polym Sci* 1988;35:1987–2000.
- [44] Moss CE, Butler MF, Müller M, Cameron RE. Submitted for publication.
- [45] Vickers ME, Briggs NP, Ibbett RN, Payne JJ, Smith SB. *Polymer* 2001;42:8241–8.
- [46] Crawshaw J, Cameron RE. *Polymer* 2000;41:4691–8.
- [47] Crawshaw J, Vickers ME, Briggs NP, Heenan RK, Cameron R. *Polymer* 2000;41:1873–81.
- [48] Mortimer SA, Peguy AA. *Cellulose Chem Technol* 1996;30:117–32.
- [49] Mortimer SA, Peguy AA, Ball RC. *Cellulose Chem Technol* 1996;30:251–66.
- [50] Mortimer SA, Peguy AA. *J Appl Polym Sci* 1996;60:305–16.
- [51] Mortimer SA, Peguy AA. *J Appl Polym Sci* 1996;60:1747–56.
- [52] Buijtenhuijs FA, Abbas M, Witteveen AI. *Papier* 1986;40:615–9.
- [53] Sabatini DD, Bensch K, Barnett RJ. *J Cell Biol* 1963;17:19–58.
- [54] Iijima H, Sogawa K, Kamide K. *Polym J* 1996;28:808–16.
- [55] Crank J. *The mathematics of diffusion*, 2nd ed. Oxford: Clarendon Press; 1975.
- [56] Cahn JW. *J Chem Phys* 1965;42:93–9.
- [57] Barton BF, Reeve JL, McHugh AJ. *J Polym Sci, Part B: Polym Phys* 1997;35:569–85.